Dynamical phase behavior of the single- and multi-lane asymmetric simple exclusion process via matrix product states

Phillip Helms,[*] Ushnish Ray,[†] and Garnet Kin-Lic Chan[‡]
Division of Chemistry and Chemical Engineering, California Institute of Technology, Pasadena, California 91125, USA

(Received 17 April 2019; published 2 August 2019)

The open asymmetric simple exclusion process (ASEP) has emerged as a paradigmatic model of nonequilibrium behavior, in part due to its complex dynamical behavior and wide physical applicability as a model of driven diffusion. We compare the dynamical phase behavior of the one-dimensional (1D) ASEP and the multi-lane ASEP, a previously unstudied extension of the 1D model that may be thought of as a finite-width strip of the fully two-dimensional (2D) system. Our characterization employs large deviation theory (LDT), matrix product states (MPS), and the density matrix renormalization group (DMRG) algorithm, to compute the current cumulant generating function and its derivatives, which serve as dynamical order parameters. We use this measure to show that when particles cannot exit or enter the lattice vertically, the phase behavior of the multi-lane ASEP mimics that of its 1D counterpart, exhibiting the macroscopic and microscopic signatures of the maximal current, shock, and high-density–low-density coexistence phases. Conversely, when particles are allowed to freely enter and exit the lattice, no such transition is observed. This contrast emphasizes the complex interplay between latitudinal and longitudinal hopping rates and the effect of current biasing. Our results support the potential of tensor networks as a framework to understand classical nonequilibrium statistical mechanics.

DOI: 10.1103/PhysRevE.100.022101

I. INTRODUCTION

In recent years, the asymmetric simple exclusion process (ASEP) has emerged as a paradigmatic model of nonequilibrium behavior in statistical mechanics [1]. The basis for this popularity resembles that of the Ising model: a simply defined model with contrastingly complex behavior and wide applicability. The ASEP is defined by bulk and boundary hopping rates that govern the stochastic movement of particles between sites on a one-dimensional (1D) lattice, limiting each site to an occupancy of one particle at most [2]. This simplistic model, originally used to study protein synthesis [3], has since been applied to understand diverse physical problems such as the transport properties of molecular motors [4], polymer reptation [5], transport through membranes [6], and surface growth [7].

Because of its simplicity and applicability, the open ASEP has been studied extensively, revealing a complex dynamical phase diagram, with both boundary and bulk driven phase transitions existing between many possible phases [8]. Additionally, many exact and semi-analytic results have been derived, making the ASEP a good candidate for benchmarking computational methods [9–12].

Much recent attention on ASEP has centered on more complex realizations of the model, such as multispecies and quantum analogs [13,14] or studies of the effects of spatial inhomogeneities [15]. In this work, we characterize the behavior of the multi-lane ASEP, which can be thought of as a finite-width strip of the fully two-dimensional (2D) model. Previously, analysis of the behavior of the multi-lane ASEP was limited to specific derivatives of the two-lane model and focused on the mean behaviors of the relevant observables, potentially missing critical details encoded by fluctuations [16–19]. Alternatively, current fluctuations in the fully 2D ASEP have been explored within macroscopic fluctuation theory, although numerical validation of the resulting expressions has been limited due to the cost of the required computations [20–22].

In this work, we provide a first step towards numerically interpolating between the behaviors of the 1D and fully 2D systems by studying the multi-lane ASEP with up to four lanes. Specifically, we work within the framework established by large deviation theory (LDT) [23–25] and compute the current cumulant generating function (CGF), whose derivatives encode fluctuations of the current and serve as dynamical order parameters.

Because of the difficulties associated with measuring rare events in large or complex systems, significant effort has been devoted to the development of appropriate and robust numerical and analytic approaches for computing large deviation functions such as the CGF. Monte Carlo sampling methods (such as the cloning algorithm and transition path sampling [26–28] augmented with importance sampling [21,29,30] and direct rate function evaluation techniques [31]) have been applied to both lattice and continuum nonequilibrium systems [9,11,26,28,32–41]. Here, we compute these functions using matrix product states (MPS) and the density matrix renormalization group (DMRG) algorithm. This approach is an example of a tensor network (TN) method, where the

[*]phelms@caltech.edu
[†]uray@caltech.edu
[‡]garnetc@caltech.edu

 ©2019 American Physical Society

high-dimensional probability distribution is represented as a contraction of many tensors. The TN approach has been used to study nonequilibrium lattice problems both analytically, via the matrix product ansatz [10,42], and computationally [9,35, 43–45]. Recently, it has been used to understand kinetically constrained models of glasses [46].

The remainder of this paper proceeds by first providing a brief introduction to large deviation theory, matrix product states, and the density matrix renormalization group algorithm. We then calibrate our implementation on the dynamical phase behavior of the 1D (single-lane) ASEP, where we find excellent agreement between our results and the semi-analytic expressions for the current cumulant generating function in the region of applicability of the functional Bethe ansatz [12,47,48]. We note that DMRG has previously been successfully used to validate expressions for high-order current cumulants of the 1D ASEP [9] and to compute critical exponents in the totally asymmetric case [35]. We also report on microscopic observables, such as the local density and activity. While the behavior of these observables has been understood from approximate theories or near various analytically tractable limits [48], the exact numerically computed quantities have typically not been reported.

We use the 1D results as a framework to extend our study to the multi-lane ASEP with up to four lanes. Here, we describe the effect of vertical hopping rates on the longitudinal dynamical phase behavior by comparing the behaviors of the closed multi-lane ASEP, where particle insertion and removal is only permitted at the horizontal boundaries, and the open multi-lane ASEP, where particles freely enter and exit the lattice vertically. The comparison of the behaviors of these models reveals the complexity of the effects of vertical hopping rates on longitudinally biased systems, and serves as a step towards understanding the fully 2D ASEP.

II. LARGE DEVIATION THEORY AND MATRIX PRODUCT STATES

We first briefly summarize some relevant concepts in large deviation theory, the theory of matrix product states, and the density matrix renormalization group. A more complete description can be found in recent reviews [25,28,49,50].

In a nonequilibrium system, the state vector $|P_t\rangle$ evolves from an initial state $|P_0\rangle$ according to a master equation with dynamics generated by a non-Hermitian Markov operator $\mathcal{W}$,

$$\partial_t |P_t\rangle = \mathcal{W}|P_t\rangle, \tag{1}$$

with the probability of a system configuration $\mathcal{C}$ at time t given by $\text{Prob}(\mathcal{C}_t) \equiv \langle \mathcal{C}|P_t\rangle$. The long-time limit yields the final (steady) state $|P_\infty\rangle$. The probability of observing a given trajectory of configurations $\mathscr{C}(t_N) = \{\mathcal{C}_0, \mathcal{C}_1, \ldots, \mathcal{C}_{t_N}\}$ at times $\{t_0, \ldots, t_N\}$ $(dt = t_N/N)$ is

$$\text{Prob}(\mathscr{C}(t_N)) = \text{Prob}(\mathcal{C}_0) \prod_{i=0}^{t_{N-1}} \langle \mathcal{C}_{i+1}|e^{dt\mathcal{W}}|\mathcal{C}_i\rangle. \tag{2}$$

We can define dynamical observables along such a trajectory, such as a time-local observable $\mathcal{O} = \sum_{i=0}^{t_{N-1}} o(\mathcal{C}_{i+1}, \mathcal{C}_i)$, with o being an arbitrary function of time-adjacent configurations ($\mathcal{C}_{i+1}$ and $\mathcal{C}_i$). To characterize the steady-state expectation value and fluctuations of this observable, we define a cumulant generating function $\psi(\lambda)$,

$$\begin{aligned}\psi(\lambda) &= \lim_{t_N\to\infty} t_N^{-1} \ln\langle e^{-\lambda\mathcal{O}}\rangle \\ &= \lim_{t_N\to\infty} t_N^{-1} \ln \sum_{\mathscr{C}(t_N)} \text{Prob}(\mathscr{C}(t_N))e^{-\lambda\mathcal{O}},\end{aligned} \tag{3}$$

where λ is a field conjugate to the observable. At $\lambda = 0$, the first derivative of ψ is the observable's steady-state expectation value $\langle o\rangle$; characterizations of the fluctuations of o, via its cumulants, are obtained from higher-order derivatives of ψ. A fundamental result in LDT is that $\psi(\lambda)$ is the largest eigenvalue E_0, of a tilted operator $\mathcal{W}_\lambda$, i.e.,

$$\mathcal{W}_\lambda|P^\lambda\rangle = \psi(\lambda)|P^\lambda\rangle, \tag{4}$$

where, for discrete configurations, the tilted operator is

$$\mathcal{W}_\lambda(\mathcal{C}, \mathcal{C}') = \mathcal{W}(\mathcal{C}, \mathcal{C}')e^{-\lambda o(\mathcal{C},\mathcal{C}')}(1 - \delta_{\mathcal{C},\mathcal{C}'}) - R(\mathcal{C})\delta_{\mathcal{C},\mathcal{C}'}, \tag{5}$$

with $R(\mathcal{C}) = \sum_{\mathcal{C}\neq\mathcal{C}'} \mathcal{W}(\mathcal{C}, \mathcal{C}')$ and with right and left eigenvectors $|P^\lambda\rangle$ and $\langle\bar{P}^\lambda|$. The eigenvectors give the configurational probabilities at initial, intermediate, and final times, respectively, being

$$\begin{aligned}\left|P^\lambda_{t_0}\right\rangle &= \frac{\text{diag}(|\bar{P}^\lambda\rangle \otimes |P^{\lambda=0}\rangle)}{\langle\bar{P}^\lambda|P^{\lambda=0}\rangle}, \\ \left|P^\lambda_{t_{\text{Int.}}}\right\rangle &= \frac{\text{diag}(|\bar{P}^\lambda\rangle \otimes |P^{\lambda}\rangle)}{\langle\bar{P}^\lambda|P^{\lambda}\rangle}, \\ \left|P^\lambda_{t_f}\right\rangle &= \frac{|P^\lambda\rangle}{\sum_C \langle C|P^\lambda\rangle},\end{aligned} \tag{6}$$

where the full trajectory satisfies $\langle\mathcal{O}\rangle = d\psi(\lambda)/d\lambda$ [51–53].

The computation of $\psi(\lambda)$ and each of the eigenvectors in Eq. (4) is achievable via exact diagonalization for only the smallest systems. Alternatively, the equation can be recast as a generalized variational problem

$$\langle\delta P^\lambda|\mathcal{W}_\lambda|P^\lambda\rangle - \psi(\lambda)\langle\delta P^\lambda|P^\lambda\rangle = 0, \tag{7}$$

where we seek to make $\psi(\lambda) = \langle P^\lambda|\mathcal{W}_\lambda|P^\lambda\rangle$ stationary with respect to a perturbation from $|P^\lambda\rangle$ to $|\delta P^\lambda\rangle$. Because $\mathcal{W}_\lambda$ is non-Hermitian, $\langle P^\lambda|\mathcal{W}_\lambda|P^\lambda\rangle$ may be above or below the exact $\psi(\lambda)$ for an approximate $|P^\lambda\rangle$ or $\langle\bar{P}^\lambda|$.

In this work, we use an MPS as an ansatz for $|P^\lambda\rangle$ and perform the optimization in Eq. (7) using the DMRG algorithm for non-Hermitian operators [43,54]. To introduce the MPS ansatz, consider a 1D lattice of length L with sites $i = 1, \ldots, L$. Each site has a local state space $\{\sigma_i\}$ of dimension d, with a system configuration $\mathcal{C}$ being an ordered list of the local states, $|\mathcal{C}\rangle = |\sigma_1, \ldots, \sigma_L\rangle$. The state vector is specified by a tensor of weights

$$|P^\lambda\rangle = \sum_{\{\sigma_1\cdots\sigma_L\}} \boldsymbol{c}_{\sigma_1,\ldots,\sigma_L}|\sigma_1, \ldots, \sigma_L\rangle, \tag{8}$$

with $\boldsymbol{c}_{\sigma_1,\ldots,\sigma_L}$ specifying the probability of the system being in configuration $|\sigma_1, \ldots, \sigma_L\rangle$.

In this exact representation, arbitrary strong correlations can exist between all sites. However, if the Markov operator $\mathcal{W}_\lambda$ only produces transitions between nearby sites, we can expect correlations to decay with distance. An efficient way

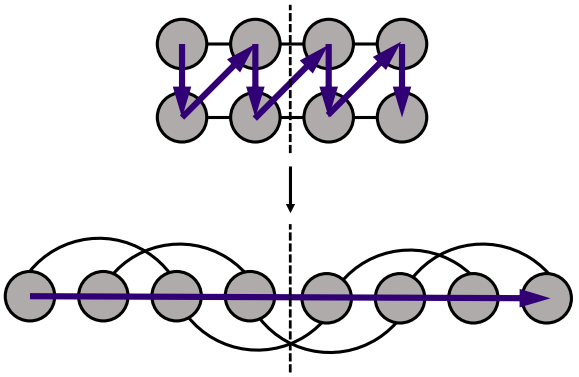

FIG. 1. A diagrammatic representation of the mapping of a 2D lattice with nearest-neighbor interactions onto a 1D lattice with long range interactions. The arrows indicate how our DMRG optimization traverses the 2D lattice and the dashed line shows the bond over which the numerical entanglement entropy is measured.

to represent states with this property is to rewrite $\boldsymbol{c}_{\sigma_1,ldots,\sigma_L}$ as a product of matrices, i.e., a matrix product state

$$|P^\lambda\rangle = \sum_{\{\sigma_1,\ldots,\sigma_L\}} \boldsymbol{M}^{\sigma_1}\boldsymbol{M}^{\sigma_2}\cdots\boldsymbol{M}^{\sigma_{L-1}}\boldsymbol{M}^{\sigma_L}|\sigma_1,\ldots,\sigma_L\rangle. \tag{9}$$

where the dimension of the matrices, also called the bond dimension D, specifies the amount of correlation that can be transmitted between sites. If we assume that D saturates with system size, then the representation is asymptotically linear in complexity with respect to system size, i.e., it contains only $O(dD^2L)$ parameters.

Matrix product states with a size-independent D are said to satisfy the 1D area law. In the quantum mechanical setting, the area law states that the entanglement entropy between two partitions of the system is proportional to the length of the boundary between them: in 1D, this is independent of system size. It is known that gapped Hamiltonians in 1D produce ground states which satisfy this law and thus can be ideally represented by matrix product states [55]. However, note that even when the area law is not satisfied, one can still exactly represent an arbitrary state with an MPS by using a sufficiently large D. For example, to satisfy the area law for a multi-lane ASEP, we can use an MPS with a D that grows exponentially with the number of lanes. In the multi-lane case, the representation also depends on the 1D traversal pattern of the sites. Here we use a zig-zag ordering of sites, shown in Fig. 1.

With $|P^\lambda\rangle$ written as an MPS, the DMRG algorithm solves the variational problem posed in Eq. (7) optimizing one $\boldsymbol{M}^{\sigma_i}$ at a time by solving an eigenproblem at each site of the form $\mathcal{W}_i^{\text{eff}}\cdot\boldsymbol{M}^{\sigma_i} = \psi(\lambda)N_i\cdot\boldsymbol{M}^{\sigma_i}$, where $\mathcal{W}_i^{\text{eff}}$ describes the action of $\mathcal{W}^\lambda$ in the vector space containing $\boldsymbol{M}^{\sigma_i}$. The metric N_i can be eliminated (i.e., converted to the identity) by using the gauge freedom in the MPS, i.e., a matrix and its inverse may be inserted between any two sites without changing $|P^\lambda\rangle$,

$$\begin{aligned} Prob(\mathcal{C}) &= \boldsymbol{M}^{\sigma_1}\boldsymbol{M}^{\sigma_2}\cdots\boldsymbol{M}^{\sigma_{L-1}}\boldsymbol{M}^{\sigma_L}, \\ &= \boldsymbol{M}^{\sigma_1}\boldsymbol{X}^{-1}\boldsymbol{X}\boldsymbol{M}^{\sigma_2}\cdots\boldsymbol{M}^{\sigma_{L-1}}\boldsymbol{M}^{\sigma_L}, \\ &= \boldsymbol{M}'^{\sigma_1}\boldsymbol{M}'^{\sigma_2}\cdots\boldsymbol{M}^{\sigma_{L-1}}\boldsymbol{M}^{\sigma_L}, \end{aligned} \tag{10}$$

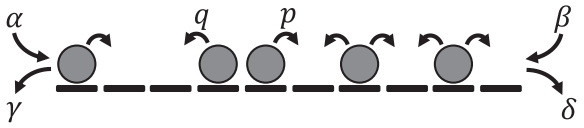

FIG. 2. The ASEP model where particles on a 1D lattice stochastically hop to a vacant neighboring right (left) site at a rate of p (q) and enter (exit) at the left and right boundaries at rates α (γ) and β (δ).

choosing the gauge to eliminate the metric yields the canonical form at the site

$$|P^\lambda\rangle = \sum_{\{\sigma_1,\ldots,\sigma_L\}} \boldsymbol{L}^{\sigma_1}\boldsymbol{L}^{\sigma_2}\cdots\boldsymbol{F}^{\sigma_i}\cdots\boldsymbol{R}^{\sigma_{L-1}}\boldsymbol{R}^{\sigma_L}|\sigma_1,\ldots,\sigma_L\rangle, \tag{11}$$

where $\sum_\sigma \boldsymbol{L}^{\sigma\,\dagger}\boldsymbol{L}^\sigma = \boldsymbol{I}$ and $\sum_\sigma \boldsymbol{R}^\sigma\boldsymbol{R}^{\sigma\,\dagger} = \boldsymbol{I}$ and $\boldsymbol{F}^{\sigma_i}$ now denotes the tensor optimized in the local eigenvalue problem. A series of sweeps of optimizations is then performed over the sites, until convergence to the targeted eigenstate of the tilted generator.

The canonical form of Eq. (11) is also used to define the bipartite entanglement entropy $S(i)$ at site i. Though entanglement is strictly a physical property of quantum systems, here the numerical value of $S(i)$ can still be used to quantify the nonfactorizable correlations between the states of sites to the left and right of site i, and to bound the maximum bond dimension required to accurately represent the state as an MPS. It can also be used as a generalized order parameter in quantum applications and may thus provide similar insights here [56,57]. By computing the singular values $\{s_m\}$ of the central $\boldsymbol{F}^{\sigma_i}_{pq}$ reshaped into the matrix $\boldsymbol{G}_{\sigma_i p,q} = \boldsymbol{F}^{\sigma_i}_{pq}$, the numerical entanglement entropy is defined as

$$S(i) = -\sum_m s_m^2 \log_2 s_m^2. \tag{12}$$

III. MODEL

The 1D ASEP (Fig. 2) takes place on a lattice of L sites. Particles hop stochastically to vacant nearest-neighbor sites at the following rates. In the lattice interior, particles hop right (left) with rate p (q) with asymmetry enforced via $p \neq q$ (ASEP). At the edges, particles enter (exit) at the left with rate α (γ) and at the right with rate β (δ). In this work, we designate the time-integrated current J for all bonds as the observable $\mathcal{O}$ mentioned previously and study phases induced by the current bias λ in the parameter regime $\alpha = \beta = \gamma = \delta = 1/2$ and $p + q = 1$. The tilted operator for the current cumulant generating function is

$$\begin{aligned} \mathcal{W}_\lambda^{\text{1D}} = {} & \alpha(e^\lambda \boldsymbol{a}_1^\dagger - \boldsymbol{v}_1) + \gamma(e^{-\lambda}\boldsymbol{a}_1 - \boldsymbol{n}_1) \\ & + \sum_{i=1}^{L-1} p(e^\lambda \boldsymbol{a}_i\boldsymbol{a}_{i+1}^\dagger - \boldsymbol{n}_i\boldsymbol{v}_{i+1}) \\ & + \sum_{i=1}^{L-1} q(e^{-\lambda}\boldsymbol{a}_i^\dagger\boldsymbol{a}_{i+1} - \boldsymbol{v}_i\boldsymbol{n}_{i+1}) \\ & + \beta(e^{-\lambda}\boldsymbol{a}_L^\dagger - \boldsymbol{v}_L) + \delta(e^\lambda \boldsymbol{a}_L - \boldsymbol{n}_L), \end{aligned} \tag{13}$$

where $\boldsymbol{a}_i$, $\boldsymbol{a}_i^\dagger$, $\boldsymbol{n}_i$, and $\boldsymbol{v}_i$ are annihilation, creation, particle number, and vacancy number operators. Note that the tilted operator is invariant with respect to the combined operation of particle-hole transformation and inversion ($\boldsymbol{a}^\dagger \leftrightarrow \boldsymbol{a}$ and $\{\ldots, i, i+1, \ldots\} \leftrightarrow \{\ldots, i+1, i, \ldots\}$). The eigenvalues of $\mathcal{W}_\lambda^{1D}$ also exhibit a Gallavotti-Cohen (GC) symmetry [51,58] of the form $\psi(\lambda) = \psi(\lambda^*)$ where, for the specified ASEP parameters, $\lambda^* = -\frac{L-1}{L+1}\ln(p/q) - \lambda$.

The multi-lane ASEP is defined on a 2D lattice of $L_y \times L_x$ sites. It augments the 1D ASEP with bulk hopping in the vertical (transverse) direction (at rates p_y, q_y) and particles inserted and removed at the vertical boundaries (at rates α_y, β_y, γ_y, δ_y). We apply the current bias in the (longitudinal) x direction, with a tilted operator that takes the form

$$\mathcal{W}_\lambda^{2D} = \mathcal{W}_\lambda^{1D_x} + \mathcal{W}_0^{1D_y}, \tag{14}$$

and retains the above GC and particle-hole and inversion symmetries. To understand the effects of the transverse parameters on the longitudinal system's phase behavior, we focus on two multi-lane parameter sets, namely open and closed vertical boundaries. Both require $p_x + q_x = 1$, $p_y = q_y = 1/2$, and $\alpha_x = \beta_x = \gamma_x = \delta_x = 1/2$, while the open (closed) case specifies $\alpha_y = \beta_y = \gamma_y = \delta_y = 1/2$ ($\alpha_y = \beta_y = \gamma_y = \delta_y = 0$).

To characterize the system, the DMRG algorithm is used to determine the largest eigenvalue of each tilted operator, through which the steady-state total current and current susceptibility are computed as $J = \partial\psi(\lambda)/d\lambda$ and $\chi = \partial^2\psi(\lambda)/d\lambda^2$. Local densities, currents, and activities may also be computed by contracting the resulting left and right eigenvector with the appropriate operator, i.e.,

$$\begin{aligned} \rho_i &= \langle P^\lambda | \boldsymbol{n}_i | P^\lambda \rangle, \\ J_i &= \langle P^\lambda | p e^{\lambda} \boldsymbol{a}_i \boldsymbol{a}_{i+1}^\dagger - q e^{-\lambda} \boldsymbol{a}_i^\dagger \boldsymbol{a}_{i+1} | P^\lambda \rangle, \\ K_i &= \langle P^\lambda | p e^{\lambda} \boldsymbol{a}_i \boldsymbol{a}_{i+1}^\dagger + q e^{-\lambda} \boldsymbol{a}_i^\dagger \boldsymbol{a}_{i+1} | P^\lambda \rangle, \end{aligned} \tag{15}$$

assuming $\langle P^\lambda | | P^\lambda \rangle = 1$.

IV. RESULTS

A. Benchmark MPS calculations of the 1D ASEP

We begin by using MPS and DMRG to characterize the phase behavior in the aforementioned parameter space and benchmark this approach against earlier results from the semi-analytical functional Bethe ansatz and approximate results from macroscopic fluctuation theory [8]. In this space, there are three expected phases, which are described in Fig. 3(a) via rudimentary sketches of both the steady-state density profile and the most probable particle configurations. These are the maximal current (MC) phase, where, in the most probable microscopic configurations, particles are evenly spaced throughout the lattice, allowing a maximal amount of biased hopping, the shock (S) phase, where particles conglomerate on one side of the lattice to form a shock that, in path-space simulations, performs a Brownian walk on the lattice, and the high-density–low-density coexistence (HD + LD) phase, where the entirely filled and empty states (with some boundary effects) are degenerate in the thermodynamic limit and correspond to a steady-state density profile of $\rho = 1/2$.

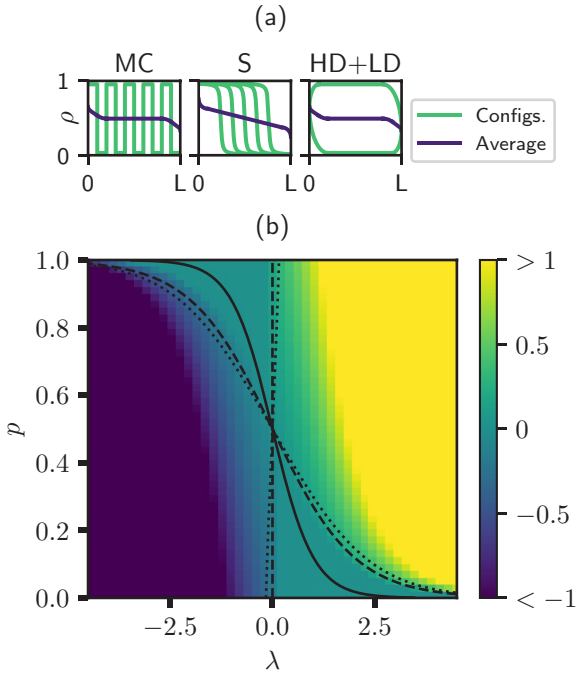

FIG. 3. (a) Rudimentary sketches of the density profiles in the three possible phases. Blue curves represent approximate steady-state density profiles while green curves depict typical particle configurations. (b) A map of the dynamical phase behavior of the ASEP showing the steady-state current J as a function of p and λ for a length $L = 20$ lattice as determined via DMRG. Additionally shown in black are lines indicating the center of the GC symmetry (solid) and the predicted boundaries between the MC and shock phases (dotted, via macroscopic fluctuation theory [8,59,60]) and the shock and HD + LD phases (dashed, via functional Bethe ansatz [8,61]).

The predicted phase diagram is mapped in Fig. 3(b) where the lines indicate the line of GC symmetry (solid), the boundary between the MC and S phases (dotted, via macroscopic fluctuation theory), and the boundary between the S and HD + LD phases (dashed, via functional Bethe ansatz). The steady-state current is also shown, computed via DMRG for an $L = 20$ ASEP, showing that current functions as a dynamical order parameter for the transition from S to HD + LD, going effectively to zero in the HD + LD phase. While the boundary between the MC and S phases is commonly defined as the point where the per site current is $J = (p - q)/4$, we are not aware of an order parameter for this transition, which instead appears as a smooth crossover in the current rather than a true phase boundary. Also note that because of the symmetries of the system, the remaining analysis can be limited to the lower left region of the parameter space ($p < 1/2$ to the left of the line of GC symmetry), with the rest of the diagram mapped out by symmetry.

Finite size errors can be converged rapidly by increasing the lattice size. In Fig. 4, we characterize this behavior using system properties such as the cumulant generating function, current, current susceptibility, and excited state gap for a range of λ near $\lambda = 0$ with $p = 0.1$ and for lattice sizes up to $L = 100$ via DMRG with bond dimension D between 50 and 300. The relative errors in the energy, current, and numerical

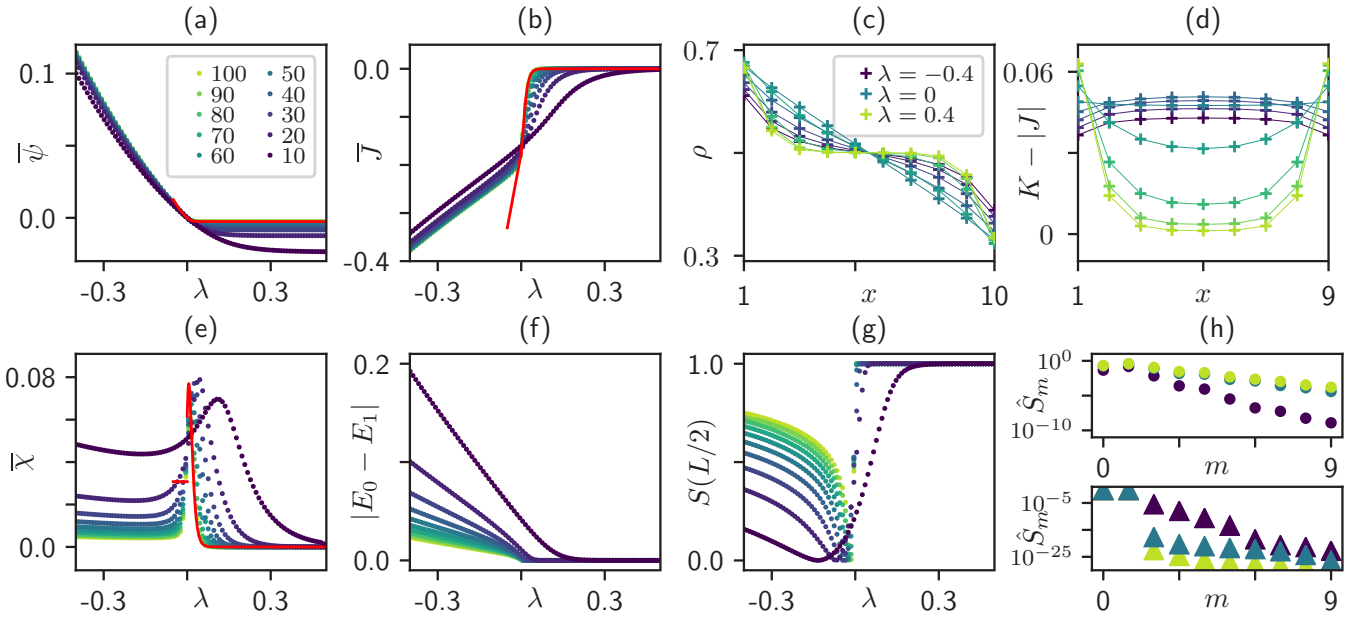

FIG. 4. The behavior of the 1D ASEP with lattice lengths of $L = [10, 100]$. The DMRG results for the normalized (a) CGF. $\overline{\psi} = E_0/L$, (b) current $\overline{J} = \partial_\lambda \psi / L$, and (e) scaled current susceptibility $\overline{\chi} = \partial_\lambda^2 \psi / L^2$ compared to the analytic functional Bethe ansatz expressions (red), valid for $\lambda \to 0^-$ and $\lambda > 0$; additionally (f) shows the gap between the first and and second largest eigenvalues E_0 and E_1. Plots (c) and (d) show the density ρ and recurrent hopping $K - |J|$ as a function of position in a $L = 10$ lattice, x, and λ. (g) The numerical entanglement entropy S of a bipartition at the center bond as a function of λ with the upper (lower) subfigures in (h) showing the corresponding ordered numerical entanglement spectrum, with $\hat{S}_m = -s_m^2 \log_2 s_m^2$, at $\lambda = -0.3$ ($\lambda = 0.3$).

entanglement entropy in the MC phase for a bond dimension of $D = 10$ are approximately, $\mathrm{Err}_E = 0.01\%$, $\mathrm{Err}_J = 0.02\%$, and $\mathrm{Err}_S = 10\%$, respectively. Increasing to a bond dimension of $D = 150$ improves these relative errors to $\mathrm{Err}_E = 0.0001\%$, $\mathrm{Err}_J = 0.001\%$, and $\mathrm{Err}_S = 0.1\%$. As a benchmark, the solid red line in Figs. 4(a), 4(b), and 4(e) corresponds to the functional Bethe ansatz result, which is valid only in the HD + LD phase and near $\lambda = 0$ in the S phase.

As $L \to \infty$, a number of interesting behaviors are observed, particularly at the interface between the S and HD + LD phases. In this region, the cumulant generating function transitions from having a finite negative slope to become nearly flat, signifying a transition into a low-current regime. This transition is marked by a continuous change in the current and an abrupt change in the current susceptibility, as shown in Fig. 4(e). Note that here the current susceptibility has been scaled by L^2, instead of L, to show that this scaled measure does not diverge at $\lambda = 0$. We also see that the system becomes gapless due to the degeneracy of the high-density and low-density configurations. This degeneracy does not cause a spike in the susceptibility because the high-density and low-density states are of the same particle-hole and inversion symmetry while $\partial_\lambda \mathcal{W}_\lambda$ is odd under this symmetry. Instead, the growing susceptibility is controlled by the second gap [between E_2 and (E_0, E_1)], which also closes at this point.

The MPS representation also provides the state's full configurational information, enabling us to study the microscopic structure of the phases and quantities that are not derivatives of the cumulant generating function. Figures 4(c) and 4(d) show the steady-state density ρ and recurrent hopping $K - |J|$, computed as specified in Eq. (15), as a function of the position in the lattice x and the current bias λ. These density profiles correspond to those shown in Fig. 3(a), with the linear profile near $\lambda = 0$ corresponding to the shock phase. The HD + LD and MC phases can here be distinguished via the rate of recurrent hopping; particles and holes are spatially dispersed in the MC phase, allowing frequent opportunities to hop back and forth, as indicated by the finite observed recurrent hopping at $\lambda < 0$. When the transition is made into the HD + LD phase, the recurrent hopping drops to nearly zero in the lattice bulk, attributable to the lattice being nearly entirely filled or empty in this phase and thus providing few opportunities for recurrent hops.

An additional way to summarize the microscopic information (and the associated correlations in the system) is via the numerical entanglement entropy and spectrum [$S(i)$ and $\{s_m\}$ in Eq. (12)] which we measure at the middle of the lattice. These are plotted for the right eigenvector $|P^\lambda\rangle$ in Fig. 4(g). There are two clear regions present in the numerical entanglement entropy, one corresponding to the MC phase, the other to the HD + LD phase. For the MC phase, the spectrum decays slowly, indicating that a relatively large bond dimension is required to accurately represent the given state. In the HD + LD phase, the numerical entanglement entropy is larger and appears to be exactly 1 ($\log_2 2$). The numerical entanglement spectrum shows that only two modes contribute, arising from the filled and empty configurations, indicating the state can be represented exactly by an MPS of bond dimension 2.

B. Multi-lane ASEP model

We now consider a system comprised of multiple ASEP lanes, with particles that may hop vertically (y direction)

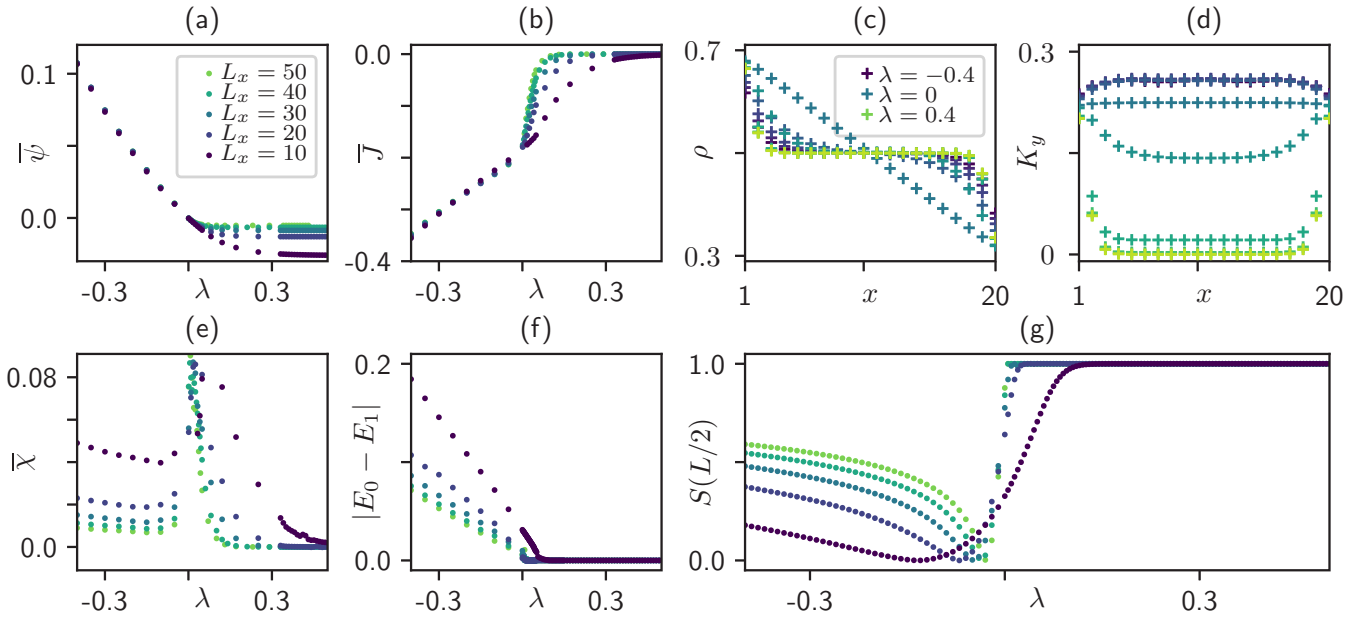

FIG. 5. The behavior of the closed multi-lane ASEP showing the DMRG results for the normalized (a) CGF $\overline{\psi} = E_0/(L_x L_y)$, (b) current $\overline{J} = \partial_\lambda \psi/(L_x L_y)$, and (e) scaled current susceptibility $\overline{\chi} = \partial_\lambda^2 \psi/(L_x^2 L_y)$ as well as (f) the gap between the first and second largest eigenvalues E_0 and E_1 for the four lane systems with lengths up to $L_x = 50$. Plots (c) and (d) show the density ρ and vertical hopping activity K_y between lanes for a two-lane ASEP with $L_x = 20$. (g) The numerical entanglement entropy S of a bipartition of the system at the center bond as a function of λ is shown.

or horizontally (x direction), where we will examine the unexplored interplay between vertical and horizontal currents that can generate new phase behavior.

1. Closed Multi-lane ASEP

A simple, but nontrivial, extension of the 1D ASEP into multiple lanes, as specified in Sec. III, is to augment horizontal hopping and entry and exit parameters with equal vertical hopping rates $p_y = q_y = 1/2$ and no entry or exit at the vertical bounds, i.e., closed boundary conditions. To understand the phase behavior here, we again carried out DMRG calculations mapping out the behavior as a function of the longitudinal current bias λ_x for fixed $p_x = 0.1$, with bond dimensions D between 50 and 300 and with system widths and lengths of up to $L_y = 4$ and $L_x = 50$.

The resulting cumulant generating function, current, current susceptibility, and first excited state gap are displayed, respectively, in Figs. 5(a), 5(b), 5(d), and 5(e) for the $L_y = 4$ ASEP (with the $L_y = [2, 3]$ results being essentially indistinguishable from these). A comparison between this figure and Fig. 4 shows no qualitative difference between the single lane and closed multi-lane ASEP. We can analyze the ground-state MPS to confirm whether the microscopic configurations in the multi-lane system correspond to those seen in 1D.

Figures 5(c) and 5(d) show the behaviors of key observables as a function of λ. Using results from a two lane calculation, Fig. 5(c) shows the density profile in one of the lanes as a function of λ, with the most notable point being the linear profile near $\lambda = 0$, indicative of a shock phase. The MC and HD + LD phases are again indistinguishable by their density profiles. As a means of distinguishing the two phases, we can use either the horizontal recurrent hopping rate profile (as done in 1D and not shown here) or the vertical activities between the two lanes as demonstrated in Fig. 5(d). Here the bulk vertical activity is near $K_y = 1/4$ per site when in the MC phase, supporting a microscopic structure where particles neighbor holes with probability 1/2 and the probability of a vertical hop when such a configuration occurs is $p_y = q_y = 1/2$. After crossing the 1D ASEP phase boundary at $\lambda = 0$, the bulk vertical activity approaches zero, indicating that hops are prevented by an entirely full or empty lattice.

This picture is further supported by the profile of the numerical entanglement entropy for the two-lane ASEP shown in Fig. 5(g), which again mimics the behavior seen for the 1D ASEP. We would usually expect the numerical entanglement entropy across the central cut to grow with the width of the system, which it appears to do in the MC phase. In the HD + LD, however, the numerical entanglement entropy is independent of the lattice width because the phase results from entirely empty and full configurations (where particle occupancy is perfectly correlated between the lanes in both configurations).

2. Open Multi-lane ASEP

To quantify the effects of vertical boundaries on the horizontally biased dynamical phase behavior of this multi-lane ASEP, we further consider a vertically open multi-lane ASEP, where vertical entry or exit rates are 1 or 2, as specified in Sec. III. In these calculations, we employed DMRG to study the ASEP behavior as a function of the horizontal bias, λ_x, near $\lambda_x = 0$, with $p_x = 0.1$ for systems of up to length $L_x = 50$ with up to three lanes ($L_y = 3$) using a maximum bond dimension of $D = 50$.

The results are displayed in Fig. 6, with the cumulant generating function, current, current susceptibility, and first

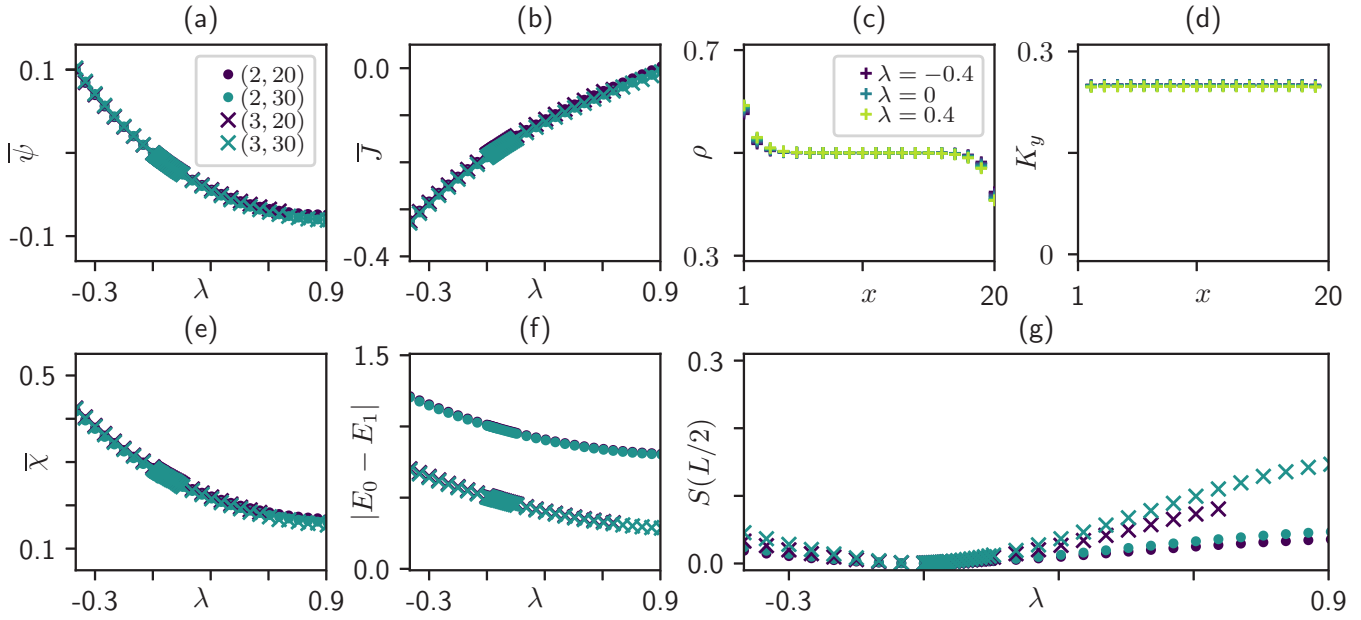

FIG. 6. The behavior of the open multi-lane ASEP showing the DMRG results for the (a) normalized CGF $\overline{\psi} = E_0/(L_x L_y)$, (b) current $\overline{J} = \partial_\lambda \psi/(L_x L_y)$, and (e) current susceptibility $\overline{\chi} = \partial_\lambda^2 \psi/(L_x L_y)$ as well as (f) the gap between the first and second largest eigenvalues E_0 and E_1 for the two- and three-lane systems with lengths up to $L_x = 30$. Plots (c) and (d) show the density ρ and vertical hopping activity K_y between lanes for a two-lane ASEP with $L_x = 20$. (g) The numerical entanglement entropy S of a bipartition of the system at the center bond as a function of λ is shown.

excited state gap being shown in Figs. 6(a), 6(b), 6(e), and 6(f). The per site macroscopic observables are nearly indistinguishable for the various system sizes, with the only noticeable difference caused by the requisite shifting of the point of GC symmetry as a function of system length. While in the closed multi-lane model the current detected a transition into the HD + LD phase, no such transition is apparent here.

This is further supported by a microscopic analysis for a lattice of size 2×20. The density and activity profiles are shown in Figs. 6(c) and 6(d) as a function of λ. The λ sweep show no changes in the behavior of the density and vertical activity. This is also true at $\lambda = 0$, where the phase transition would be expected to occur. While the steady-state number of hops between lattice sites does not seem to indicate any phase transition, we note that the desired low current behavior is created in a MC-like density profile by causing a small current to flow to the left in the bulk to counter the large current flowing to the right at the boundaries. This also illustrates a significant difference between the single-lane and multi-lane systems, namely that the steady-state current need not be spatially homogenous.

The lack of the phase transition in the open multi-lane system contrasts with the behavior of the closed multi-lane system. The behavior of the open model likely arises due to the availability of a vertical particle bath that enables rapid relaxation when jammed phases begin to form.

V. CONCLUSION

In conclusion, we use MPS and DMRG to conduct a systematic study of the 1D and multi-lane ASEP with open horizontal boundary conditions under a current bias. With regards to the physics of the ASEP, we characterized the phase transition between the MC and HD + LD phases in the 1D system, showing agreement for the current cumulant generating function with known semi-analytic expressions and demonstrating changes in underlying microscopic structure via the steady-state density and activity profiles. We additionally found that the numerical entanglement entropy and spectrum, though different in physical meaning to their quantum counterparts, provide a global summary of the correlations in the system, identifying the sharp structure of the transition into the HD + LD phase. In the case of the multi-lane ASEP, we demonstrated that when biasing the current longitudinally with a simple choice of vertical hopping rates the development of the HD + LD phase occurs when vertical particle entry or exit is prohibited, but the phase boundary disappears entirely when this is reintroduced. This emphasizes the complex interplay between vertical and horizontal hopping parameters in this class of boundary driven processes and calls for the development of a more complete understanding of the multi-lane and fully 2D ASEP.

The TN methods used in this work are numerical realizations of the matrix product ansatz, which has long been used to produce semi-analytical solutions in driven lattice models. As we show, the flexibility of the numerical approach allows this framework to be applied to problems where analytical techniques are difficult to use, as demonstrated here with the multi-lane ASEP. In addition to providing a simple numerical route to compute large deviation functions, this approach also provide access to details of the underlying microscopic configurations, all without encountering the limitations of analytic methods or the sampling difficulties that plague Monte Carlo techniques. In addition, the success seen here and in other recent work [46] indicates the potential of more general tensor network approaches, which allow for a

natural treatment of two-dimensional, three-dimensional, and thermodynamic lattice systems [62–64]. Currently, the TN methods remain challenging to apply to continuum systems. Continuing to further the application of tensor networks to nonequilibrium statistical models thus remains an exciting area of ongoing research.

ACKNOWLEDGMENTS

This work was supported primarily by the US National Science Foundation (NSF) via Grant No. CHE-1665333. P.H. was also supported by a NSF Graduate Research Fellowship under Grant No. DGE-1745301 and an ARCS Foundation Award.

[1] T. Chou, K. Mallick, and R. Zia, Rep. Prog. Phys. **74**, 116601 (2011).
[2] B. Schmittmann and R. K. Zia, Phase Transitions Crit. Phenom. **17**, 3 (1995).
[3] F. Spitzer, Adv. Math. **5**, 246 (1970).
[4] S. Klumpp and R. Lipowsky, J. Stat. Phys. **113**, 233 (2003).
[5] B. Widom, J. L. Viovy, and A. D. Defontaines, J. Phys. I **1**, 1759 (1991).
[6] K. Heckmann, *Single File Diffusion* (Springer US, Boston, MA, 1972), pp. 127–153.
[7] J. Krug, Adv. Phys. **46**, 139 (1997).
[8] A. Lazarescu, J. Phys. A **48**, 503001 (2015).
[9] M. Gorissen, A. Lazarescu, K. Mallick, and C. Vanderzande, Phys. Rev. Lett. **109**, 170601 (2012).
[10] B. Derrida, M. R. Evans, V. Hakim, and V. Pasquier, J. Phys. A **26**, 1493 (1993).
[11] B. Derrida, J. L. Lebowitz, and E. R. Speer, J. Stat. Phys. **110**, 775 (2003).
[12] B. Derrida and J. L. Lebowitz, Phys. Rev. Lett. **80**, 209 (1998).
[13] N. Crampe, C. Finn, E. Ragoucy, and M. Vanicat, J. Phys. A **49**, 375201 (2016).
[14] D. Bernard and T. Jin, arXiv:1904.01406.
[15] A. Lazarescu, J. Phys. A **50**, 254004 (2017).
[16] A. K. Verma and A. K. Gupta, J. Phys. Commun. **2**, 045020 (2018).
[17] Z. Ding, T. Liu, X. Lou, Z. Shen, K. Zhu, R. Jiang, B. Wang, and B. Chen, Physica A (Amsterdam) **516**, 317 (2019).
[18] H. Yamamoto, D. Yanagisawa, and K. Nishinari, arXiv:1904.03988.
[19] I. Dhiman and A. K. Gupta, Int. J. Mod. Phys. C **29**, 1850037 (2018).
[20] Z.-J. Ding, S.-L. Yu, K. Zhu, J.-X. Ding, B. Chen, Q. Shi, X.-S. Lu, R. Jiang, and B.-H. Wang, Physica A (Amsterdam) **492**, 1700 (2018).
[21] U. Ray, G. K.-L. Chan, and D. T. Limmer, Phys. Rev. Lett. **120**, 210602 (2018).
[22] C. Pérez-Espigares and P. I. Hurtado, arXiv:1902.01276.
[23] M. Donsker and S. Varadhan, Commun. Pure Appl. Math. **28**, 1 (1975).
[24] R. S. Ellis, *Entropy, Large Deviations, and Statistical Mechanics* (Springer, New York, 1985).
[25] H. Touchette, Phys. Rep. **478**, 1 (2009).
[26] A. Lasanta, P. I. Hurtado, and A. Prados, Eur. Phys. J. E **39**, 35 (2016).
[27] T. Nemoto, R. L. Jack, and V. Lecomte, Phys. Rev. Lett. **118**, 115702 (2017).
[28] U. Ray, G. K.-L. Chan, and D. T. Limmer, J. Chem. Phys. **148**, 124120 (2018).
[29] T. Nemoto, F. Bouchet, R. L. Jack, and V. Lecomte, Phys. Rev. E **93**, 062123 (2016).
[30] K. Klymko, P. L. Geissler, J. P. Garrahan, and S. Whitelam, Phys. Rev. E **97**, 032123 (2018).
[31] D. Jacobson and S. Whitelam, arXiv:1903.06098.
[32] T. Bodineau and B. Derrida, Phys. Rev. E **72**, 066110 (2005).
[33] J. P. Garrahan, R. L. Jack, V. Lecomte, E. Pitard, K. van Duijvendijk, and F. van Wijland, J. Phys. A **42**, 075007 (2009).
[34] J. de Gier and F. H. L. Essler, Phys. Rev. Lett. **107**, 010602 (2011).
[35] M. Gorissen and C. Vanderzande, J. Phys. A **44**, 115005 (2011).
[36] A. Prados, A. Lasanta, and P. I. Hurtado, Phys. Rev. E **86**, 031134 (2012).
[37] F. Carollo, J. P. Garrahan, and I. Lesanovsky, Phys. Rev. B **98**, 094301 (2018).
[38] T. Brewer, S. R. Clark, R. Bradford, and R. L. Jack, J. Stat. Mech.: Theory Exp. (2018) 053204.
[39] A. J. Schile and D. T. Limmer, J. Chem. Phys. **149**, 214109 (2018).
[40] T. GrandPre and D. T. Limmer, Phys. Rev. E **98**, 060601(R) (2018).
[41] C. Y. Gao and D. T. Limmer, AIP J. Chem. Phys. **151**, 014101 (2019).
[42] R. A. Blythe and M. R. Evans, J. Phys. A **40**, R333 (2007).
[43] E. Carlon, M. Henkel, and U. Schollwöck, Eur. Phys. J. B **12**, 99 (1999).
[44] M. Gorissen, J. Hooyberghs, and C. Vanderzande, Phys. Rev. E **79**, 020101(R) (2009).
[45] T. H. Johnson, S. R. Clark, and D. Jaksch, Phys. Rev. E **82**, 036702 (2010).
[46] M. C. Bañuls and J. P. Garrahan, arXiv:1903.01570.
[47] S. Prolhac, arXiv:0904.2356.
[48] A. Lazarescu and V. Pasquier, J. Phys. A **47**, 295202 (2014).
[49] H. Touchette, arXiv:1106.4146.
[50] U. Schollwöck, Ann. Phys. (NY) **326**, 96 (2011).
[51] J. L. Lebowitz and H. Spohn, J. Stat. Phys. **95**, 333 (1999).
[52] B. Derrida and T. Sadhu, J. Stat. Phys. (2019), doi: 10.1007/s10955-019-02321-4.
[53] B. Derrida and T. Sadhu, arXiv:1905.07175.
[54] G. K.-L. Chan and T. Van Voorhis, J. Chem. Phys. **122**, 204101 (2005).
[55] M. B. Hastings, J. Stat. Mech.: Theory Exp. (2007) P08024.
[56] A. Kitaev and J. Preskill, Phys. Rev. Lett. **96**, 110404 (2006).
[57] F. Pollmann, A. M. Turner, E. Berg, and M. Oshikawa, Phys. Rev. B **81**, 064439 (2010).
[58] G. Gallavotti and E. G. D. Cohen, J. Stat. Phys. **80**, 931 (1995).
[59] L. Bertini, A. De Sole, D. Gabrielli, G. Jona-Lasinio, and C. Landim, J. Stat. Phys. **107**, 635 (2002).
[60] L. Bertini, A. De Sole, D. Gabrielli, G. Jona-Lasinio, and C. Landim, Rev. Mod. Phys. **87**, 593 (2015).
[61] S. Prolhac and K. Mallick, J. Phys. A **41**, 175002 (2008).
[62] F. Verstraete, V. Murg, and J. I. Cirac, Adv. Phys. **57**, 143 (2008).
[63] R. Orús, Ann. Phys. (NY) **349**, 117 (2014).
[64] H. N. Phien, J. A. Bengua, H. D. Tuan, P. Corboz, and R. Orús, Phys. Rev. B **92**, 035142 (2015).